JGR Solid Earth

RESEARCH ARTICLE
10.1029/2021JB022190

Key Points:

- We develop a new 2-D dense-array-based inversion method using receiver function travel times
- The depth extent and V_p/V_s ratio are obtained beneath the Chenghai fault within the Binchuan basin from the proposed method
- Our new method can be used to image sedimentary basin or other shallow low velocity structure using dense arrays

Supporting Information:

Supporting Information may be found in the online version of this article.

Correspondence to:

H. Yang,
hyang@cuhk.edu.hk

Citation:

Jiang, X., Hu, S., & Yang, H. (2021). Depth extent and V_p/V_s ratio of the Chenghai fault zone, Yunnan, China constrained from dense-array-based teleseismic receiver functions. *Journal of Geophysical Research: Solid Earth*, *126*, e2021JB022190. https://doi.org/10.1029/2021JB022190

Received 7 APR 2021
Accepted 4 AUG 2021

Depth Extent and V_p/V_s Ratio of the Chenghai Fault Zone, Yunnan, China Constrained From Dense-Array-Based Teleseismic Receiver Functions

Xiaohuan Jiang[1], Shaoqian Hu[2], and Hongfeng Yang[3,1]

[1]Shenzhen Research Institute, the Chinese University of Hong Kong, Shenzhen, China, [2]Subsurface Multi-Scale Imaging Key Laboratory of Hubei Province, Institute of Geophysics and Geomatics, China University of Geosciences, Wuhan, China, [3]Earth System Science Programme, the Chinese University of Hong Kong, Hong Kong, China

Abstract Fault zone (FZ) structure is critical for understanding earthquake rupture propagation and assessment of seismic hazard. In this study, we develop a new 2-D dense-array-based inversion method to obtain high-resolution FZ structure model using teleseismic receiver function. In our method, coherent travel times of converted waves and their multiples are first identified from teleseismic receiver functions; then the travel times are inverted for both depth extent and V_p/V_s ratio beneath the seismic dense array. Synthetic tests with various shallow low-velocity-zone (LVZ) models demonstrate the effectiveness and robustness of our new method. We apply our method to the data recorded by a linear dense array across the southern segment of the Chenghai fault (CHF) in Yunnan, southwestern China. The inversion results suggest that the depth of the LVZ beneath the CHF extends to ~1.1 km. Furthermore, we derive the V_p/V_s ratio simultaneously and obtain the *P*-wave velocity model from a *S*-wave velocity model of the LVZ that were derived from ambient noise tomography. Travel times predicted by the newly obtained model are consistent with teleseismic *P*- and *S*-wave arrivals. In addition, our method shows clear improvement in stability compared with the single-station H-κ method. With dense seismic arrays deployed globally, our method would be a useful tool in shallow low-velocity structure imaging studies, including fault zones and sedimentary basins.

Plain Language Summary High-resolution fault zone (FZ) structure and evolution are critical to understand earthquake physics. A number of seismic methods have been used to determine the geometry and seismic velocity drop of the LVZ, but all suffer in resolving the depth extent. Here we develop a new dense-array-based receiver function travel-time inversion method to image the low velocity zone (LVZ) of the Chenghai fault (CHF) using a linear 8-km dense across-fault array. By incorporating both converted waves and their multiples, this method can obtain LVZ depth extent and Vp/Vs ratio simultaneously. The result shows that the LVZ extends to 1.1 km, shallower than the previous result from ambient noise tomography. The travel times predicted by the inverted model have good consistency with the observations. In addition to constraining the LVZ depth of fault zones, our method is also applicable to image shallow sedimentary basins using seismic dense arrays.

1. Introduction

Earthquake rupture propagation is controlled by many factors of seismogenic faults, such as geometrical complexity (e.g., Oglesby & Archuleta, 2000; Oglesby & Mai, 2012; Yang et al., 2013; H. Yu et al., 2018), frictional properties (e.g., Weng & Yang, 2018; Yao & Yang, 2020), heterogeneous stress distribution (e.g., Duan & Oglesby, 2007; Kame et al., 2003; Weng et al., 2015; Yang et al., 2012, 2019) and crustal fault zone (FZ) structures (e.g., Ampuero & Vilotte, 2002; Harris & Day, 1997; Huang & Ampuero, 2011; Y. Huang et al., 2014; Weng et al., 2016). Surrounding the sliding interface, there often is a low velocity zone (LVZ) relative to the host rocks in fault zones, characterizing either the presence of damaged zones or sedimentary materials that were associated with fault evolution (e.g., Ben-Zion & Sammis, 2003). The width, degree of damage and depth extent of the damaged zone are important to estimate the size of potential future ruptures (e.g., Yang, 2015). Distribution of the low velocity material is critical to amplify ground motion during earthquakes (e.g., Avallone et al., 2014; Kurzon et al., 2014; Wu et al., 2009) and may thus lead to biased estimations of frictional properties on seismogenic faults (X. Chen et al., 2021; Chen & Yang, 2020). Therefore,

determination of the LVZ geometry, including its width and depth extent, and seismic structure such as the velocity contrast and V_p/V_s ratio relative to the host rocks, is important for assessment of seismic hazard.

A number of seismic methods, including modeling fault zone trapped waves, body waves and ambient noise tomography, have been used to determine the geometry and seismic velocity drop of the LVZ. Most of these methods, however, can poorly constrain the depth extent of the LVZ, and usually assume a constant V_p/V_s ratio. For instance, there is a well-known debate on the LVZ depth extent by modeling the FZ trapped waves (e.g., Ben-Zion & Sammis, 2003; Lewis et al., 2005; Li et al., 1990, 2004; Peng et al., 2003). Although modeling body waves diffracted by the LVZ can robustly constrain the depth (Yang & Zhu, 2010), high-quality waveforms of diffracted waves are not widely observed. Ambient noise tomography has relatively high lateral resolution, but is not sensitive to the sharp velocity boundaries in vertical direction and the sensitivity kernel is also limited in depth within the LVZ (e.g., Lin et al., 2013; Mordret et al., 2019; Roux et al., 2016; Y. Wang et al., 2017; Yang et al., 2020; Zhang & Gerstoft, 2014; Zigone et al., 2014, 2019). Some other methods, including the analysis of amplitude ratio of FZ-trapped waves (Y. Huang et al., 2020), can be used to constrain the shear wave velocity in the LVZ layer, but all suffer in resolving the depth extent. Furthermore, the assumption of a constant V_p/V_s ratio across the FZ may potentially affect the determination of the LVZ geometry and the velocity contrast.

On the other hand, teleseismic receiver function (RF) mainly contains *P*-to-*S* converted phases and their multiples, and is sensitive to seismic velocity discontinuities in depth as well as V_p/V_s ratio (e.g., Langston, 1979; Vinnik, 1977; Zhu & Kanamori, 2000). While the RF method has been routinely used to image structures in crust and upper mantle, it is recognized that the shallow low-velocity structure often causes strong multiple reverberations in the RF time series, and may significantly interfere with the Moho *Ps* signals (e.g., Langston, 2011; Y. Yu et al., 2015; Zelt & Ellis, 1999). As shown in previous studies, standard RF analysis may mischaracterize crustal thickness by more than 10 km based on *Ps*-phase delay beneath deep basins without accounting for shallow low-velocity layers (Yeck et al., 2013). Therefore, the phases related to sediment, or LVZ in shallow crust, are usually regarded as noise and thus are removed (e.g., Y. Yu et al., 2015). In contrast, to analyze the shallow sedimentary structure in the scale of sediment, some studies extended the original H-κ method (Zhu & Kanamori, 2000) to consider the sediment effects (e.g., Cunningham & Lekic, 2019; Tao et al., 2014; Yeck et al., 2013; Y. Yu et al., 2015). However, these extended H-κ stacking methods are only applicable to data recorded by a single station, which may be unstable and difficult to identify the converted phases that are critical for the shallow structure.

With the deployment of densely distributed seismic arrays, newly developed approaches are used to image low-velocity fault zone structures (e.g., Cunningham & Lekic, 2020; Jiang et al., 2019; Wang, Yang, et al., 2015; Ward et al., 2018; Yang et al., 2020). Specifically, a densely distributed seismic array (8 km) was deployed across the Chenghai fault (CHF) in the Binchuan basin (BCB) (Figure 1a). There is a profound LVZ associated with the CHF, 3.4 km in width, which was interpreted as the sediment deposit controlled by the fault movement and potential fault damage (Yang et al., 2020). Although it is not the specific fault damage zone which often has a width of a few hundreds of meters (Yang, 2015), the LVZ is a result of fault evolution. Furthermore, to distinguish the LVZ from the BCB, we here term it as "fault zone," rather than sedimentary basin because the Binchuan basin is indeed in a larger scale than the aperture of our dense array. The depth extent of the LVZ was estimated to be 1.5 km. However, the sensitivity kernel of surface wave dispersion in depth was no more than ~1 km within the LVZ, making it difficult to judge the reliability of the inferred depth extent. Furthermore, only a *S*-wave velocity model was obtained from ambient noise tomography, whose predicted travel times did not exactly match observations of teleseismic earthquakes (Yang et al., 2020). Deriving an independent *P*-wave velocity model and the depth extent of the LVZ is thus highly desired.

In this study, we develop a new dense-array-based RF travel-time inversion method to image the LVZ of the CHF using a linear dense across-fault array. By incorporating both converted waves and their multiples, this method can obtain LVZ depth extent and V_p/V_s ratio simultaneously (Section 4.1). We calculate the predicted travel times of teleseismic *P*- and *S*-waves using our newly obtained models, and find good consistency with the observations (Section 4.2). We also compare our results with the single-station H-κ method (Section 5.1). Moreover, we conduct extensive synthetic tests to investigate some influencing factors on the accuracy of our method, including the interference of Moho converted P_ms waves (Section 3.3), the existence of

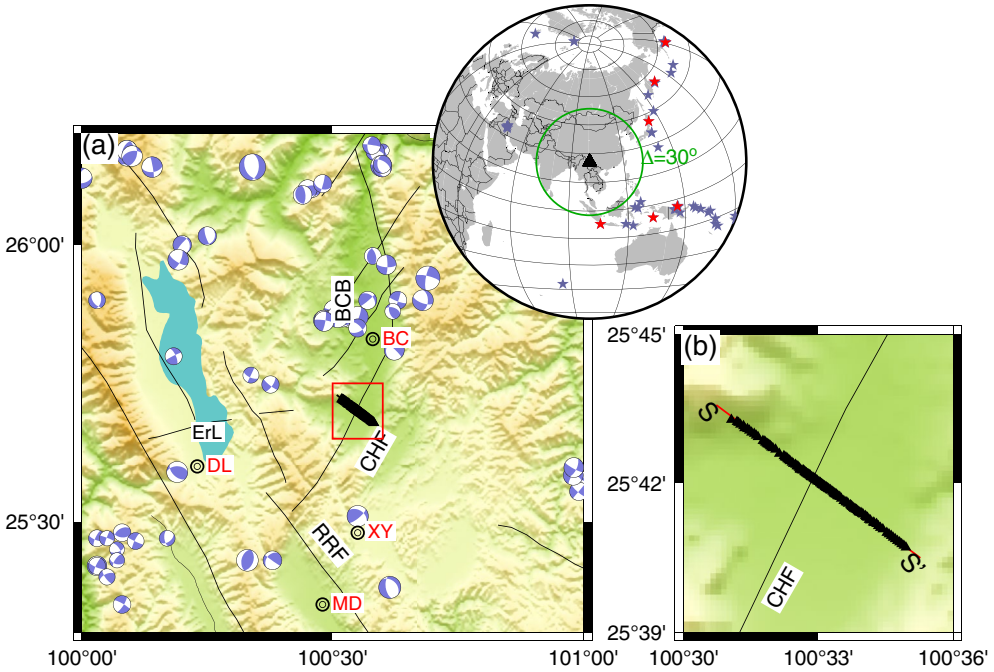

Figure 1. (a) Location of the seismic array and regional faults (black lines) in the study area. ErL: Erhai Lake, BCB: Binchuan Basin, CHF: Chenghai Fault, RRF: Red River Fault. The red box denotes the region of the linear seismic array shown in (b). The beach balls are the moment tensor solutions of regional earthquakes with $M_w > 2$ during the year of 2000–2014 (Xu et al., 2020). The black circles denote main cities in the study area: BC: Binchuan, DL: Dali, XY: Xiangyun, MD: Midu. The stars in the inset map are the locations of 56 good-quality teleseismic earthquakes with magnitudes larger than five in the epicentral distance ranging 30°–95° (blue stars), among which there are six events recorded by more than 95 stations (red stars). (b) A linear dense array with 125 short-period seismograms across the CHF. The black solid triangles denote the locations of stations.

random noise (Section 3.3), the choice of initial *S*-wave velocity model (Section 5.2), and the discrepancy of the background V_s model (Section 5.2). In addition to constraining the LVZ depth of fault zones, our method is also applicable to image shallow sedimentary basins using seismic dense arrays.

2. Data

The CHF, with a length of ~200 km in the north-south direction, is located in a seismically active region in western Yunnan province, China. The CHF starts from Yongsheng in the north and intersects with the northwest-southeast (NW-SE) trending Red River Fault (RRF) in the south. Several damaging earthquakes, including the 1,515 M_w $7^3/_4$ Yongsheng earthquake, occurred along the CHF (Wang, Wu, et al., 2015; Zhou et al., 2004). In recent years, several moderate earthquakes ($M_w < 5.0$), mostly with strike-slip focal mechanisms, occurred in the northern segment of the CHF (Xu et al., 2020) (Figure 1a). The latest moderate earthquake is the M_w 4.9 earthquake that occurred on 21 July 2019 at Yongsheng. The southern segment, however, seems less active, but is considered to be a "seismic gap" and thus a major potential source for seismic hazard (X. Huang et al., 2018) (Figure 1a).

Waveform data in this study were collected from a linear dense array across the CHF. The dense seismic array, which is consisted of 125 short-period three-component instruments (corner frequency of 5 s) with a total length of 8 km and interstation spacing of ~40 m, was deployed across the southern segment of the CHF during January–February 2018 (Yang et al., 2020) (Figure 1b). Such an ultra-dense array provides an unprecedented opportunity to investigate the CHF properties with a variety of methods.

We first process the waveform data to compute the teleseismic receiver functions. In detail, we select teleseismic events of magnitudes larger than five, which are located at epicentral distances ranging 30°–95°. For each station, we cut the continuous waveforms with a time window between 50 s before and 150 s after

Table 1
Parameters of the Six Earthquakes Used in This Study

Origin time	Latitude	Longitude	Depth	Magnitude
2018-01-18 17:48:39.770	132.8132	−6.3907	26.95	5.6
2018-01-23 06:34:54.980	105.9632	−7.0924	48.19	5.9
2018-01-23 09:31:40.890	−149.166	56.0039	14.06	7.9
2018-01-24 10:51:19.090	142.4323	41.1034	31.00	6.3
2018-01-25 02:10:34.820	166.4497	55.5423	11.15	6.2
2018-01-26 22:47:57.760	145.8477	−3.5138	10.00	6.3

theoretical *P* wave arrivals that are calculated from the global 1-D IASP91 model (Kennett & Engdahl, 1991). Then we remove linear trends, resample the waveforms to 10 Hz, and filter the waveform data with a band-pass filter of 0.05–2 Hz. As a quality control, for every event, we calculate the cross-correlation coefficients between the Z-component waveforms of each individual station with all other stations, and discard the recordings with an average coefficient lower than 0.7. We also manually pick the Z-component waveforms with clear first *P* arrivals. Then we construct RF waveforms using the time domain iteration deconvolution method (Ligorria & Ammon, 1999), with a Gaussian low-pass filter parameter of three (center frequency ~1 Hz) to suppress high-frequency noise. In total, we obtain 56 teleseismic events (blue stars in Figure 1a) of high-quality RFs. Among these events, six events recorded by more than 95 stations (red stars in Figure 1a) in our dense array are used for further analysis. Detailed parameters of these six earthquakes are listed in Table 1.

3. Method

In the RF waveforms recorded by the dense seismic array, coherent *P*-to-*S* converted phases caused by shallow low-velocity structure can be identified across the entire array (dashed lines in Figures 2a and 2b). It seems possible to pick the arrival times of the primary and secondary converted *P*-to-*S* phases (P_bs, P_bpPs) caused by the LVZ, which can then be used to constrain the shallow structure. Therefore, our method mainly includes two steps. The first step is to pick the reliable arrival times of P_bs and P_bpPs, and the second step is the dense-array-based inversion for LVZ structure. In this section, we describe each step and briefly

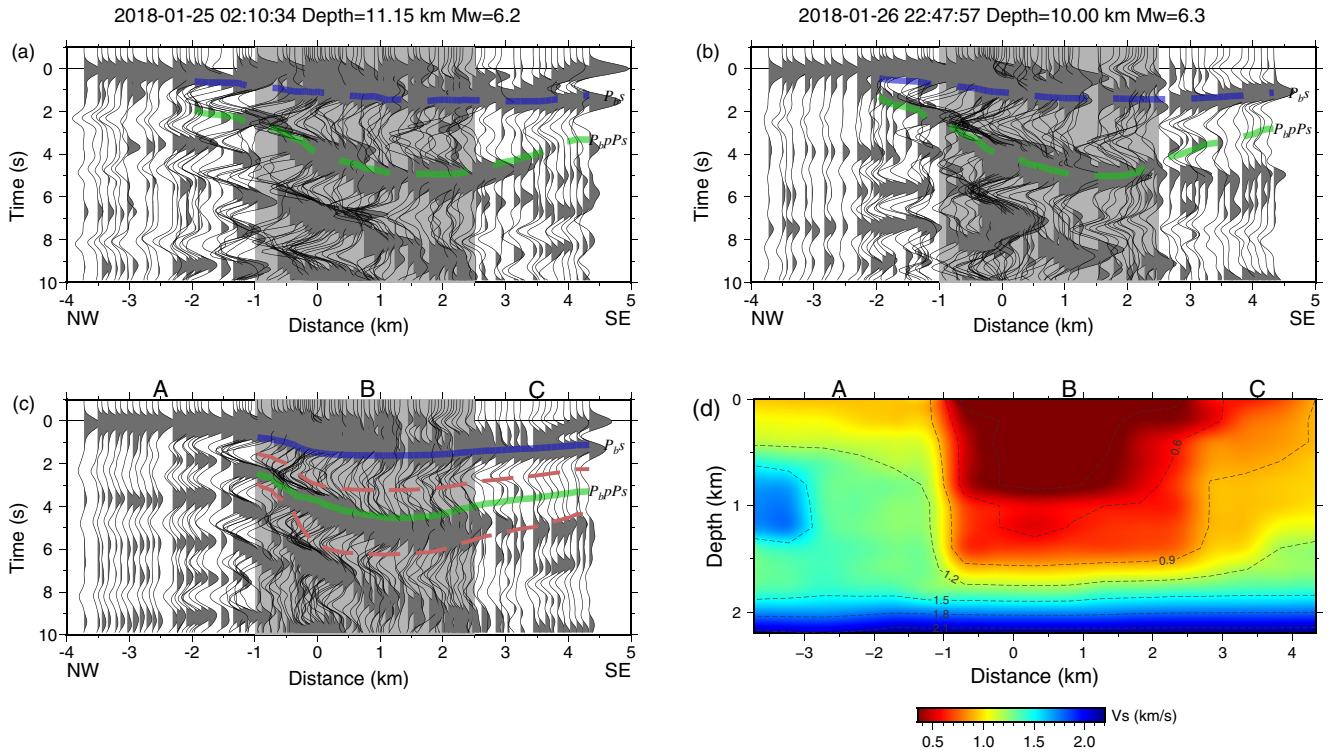

Figure 2. (a and b) Receiver function (RF) waveforms of two teleseismic events. The blue and green dashed lines represent the P_bs and P_bpPs arrivals for individual events, respectively. (c) The stacked RFs of 6 teleseismic events. The blue and green lines represent picked P_bs and P_bpPs arrivals, respectively. The red dashed lines denote the possible range of P_bpPs phase arrivals based on Equation 3. The light-gray shadow denotes the inferred LVZ region (~−1–2.4 km). (d) The *S*-wave velocity model beneath the seismic array derived from ambient noise tomography (Yang et al., 2020).

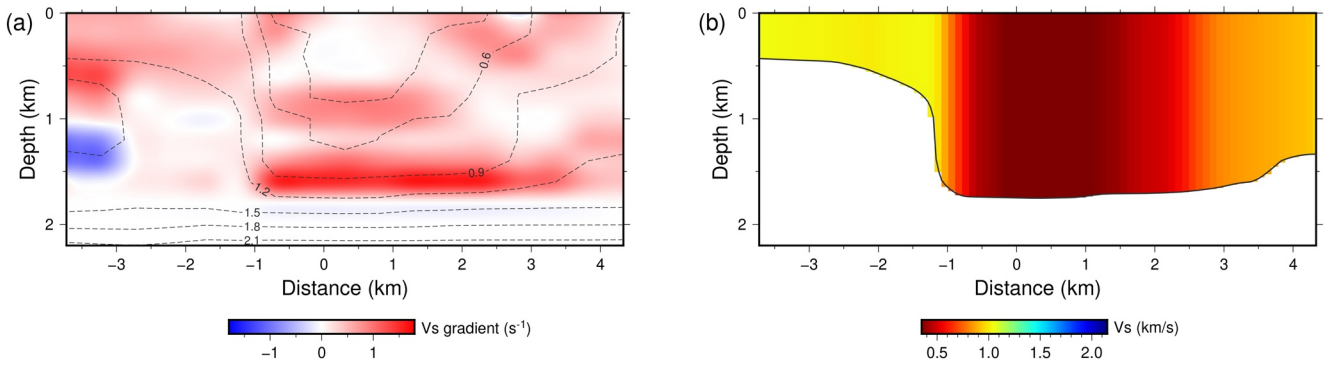

Figure 3. (a) The *S*-wave velocity vertical gradient for the V_s model in Figure 2d. The black dashed lines are the V_s contours from Figure 2d. (b) The depth-average *S*-wave velocity model of the low-velocity-zone layer obtained from Figure 2d, which serves as the background velocity model for the array-based inversion.

introduce the theoretical background. We also perform several synthetic tests to demonstrate the validation and robustness of our method.

3.1. Picking Arrival Times of P_bs and P_bpPs Phases

One key step of our method is to accurately pick P_bs and P_bpPs arrival times (t_{P_bs} and t_{P_bpPs}) from RF waveforms. It is noteworthy there is trade-off between the resolution and robustness in picking arrivals of phases. For instance, appropriate frequency range needs to be chosen, because RF waveforms in higher frequencies contain more noise despite the higher resolution. On the other hand, waveform stacking to suppress the noise is necessary, because it seems difficult to robustly identify the P_bs and P_bpPs arrivals from individual RFs of a single event (Figures 2a and 2b) (RFs of another four events are shown in Figure S1).

We conduct a trial-and-error process and choose RFs with a center frequency of ~1 Hz to ensure clear LVZ-related phases. We then linearly stack all the selected 6 events (Table 1) in this frequency range for each station, after moveout correction using a common ray parameter of 0.06 s/km (Figure 2c).

Yang et al. (2020) reports the width of this LVZ as ~3.4 km, by tracking the velocity contour of 600 m/s in the V_s model that was derived from ambient noise tomography (Figure 2d). We therefore partition the cross-section into three parts (labeled as A, B, C in Figures 2c and 2d). Region A is in the northwestern side (N-W) (<−1 km), region B is characterized as the LVZ (−1 to 2.4 km), and region C is in the southeastern side (S-E) (>2.4 km).

In the tomography results (Figure 2d), the velocity gradient in the vertical direction is larger in region A than that in region C (Figure 3a). In addition, the *P*-to-*S* phases caused by the shallow low-velocity layers in region A is too weak to be picked in the RF waveform data, possibly due to the small layer thickness (Figure 2d). Thus, we just use the stacked RFs to study the LVZ below regions B and C.

To identify the correct P_bs phases from the stacked RFs, we pick the first largest amplitude after the direct *P* arrival in the RF waveform profile (blue line in Figure 2c). For the RFs with more than one obvious phase after the first *P* arrival, we select the one closest to the largest trough as P_bs phases of the LVZ, which may indicate the bottom of the sediment layer. According to the above strategy, the P_bs phases can be traced in most stations on the RF waveforms in regions B and C (blue lines Figure 2c).

The P_bpPs phase is also difficult to distinguish from all other coherent phases in the RF waveforms directly, therefore the following relation is applied as an auxiliary constraint. The relative arrival time of P_bs and P_bpPs phases are (Zhu & Kanamori, 2000),

$$t_{P_bs} = H\left(\sqrt{\frac{1}{V_s^2} - p^2} - \sqrt{\frac{1}{(V_s\kappa)^2} - p^2}\right), \quad (1)$$

$$t_{P_bpPs} = H\left(\sqrt{\frac{1}{V_s^2} - p^2} + \sqrt{\frac{1}{(V_s\kappa)^2} - p^2}\right), \tag{2}$$

where H is the depth extent of the LVZ, V_s is shear wave velocity, p is ray parameter, and κ is the V_p/V_s ratio.

To give a reasonable range for picking P_bpPs phases in RFs, we utilize the low values of the V_s and V_p in the LVZ. That is, $p \ll 1/V_p, 1/V_s$, and thus approximately we have $p \approx 0$. Integrating Equations 1 and 2, we have,

$$\frac{t_{P_bpPs}}{t_{P_bs}} = \frac{\kappa + 1}{\kappa - 1}. \tag{3}$$

The above equation indicates that once t_{P_bs} can be reliably picked, the variation range of t_{P_bpPs} can be estimated. According to previous studies on shallow low-velocity basins (e.g., Bao & Niu, 2017; Brocher, 2005; Langston, 2004, 2011; Yeck et al., 2013), we assume κ of the LVZ within the range of 1.7–3.0, so that the t_{P_bpPs} / t_{P_bs} is within the range of 2.0–3.86. Then we pick the maximum amplitudes in the time window with the above constraint from the stacked RFs (red dashed lines in Figure 2c) as the P_bpPs phases (green lines in Figure 2c). In practice, the arrivals of the corresponding phases in the six individual events are also referred (Figures 2a, 2b, and S1). Indeed, coherent P_bpPs phases within region B are evident in the RF waveforms, while they become obscured in region C and consequently uncertainties for picking these phases in region C get greater (Figure 2c).

Note that in this step, the correctness of the P_bs identification is simply hypothesized. Indeed, it is quite difficult to determine which of the phases are the P_bs and its corresponding multiples directly from the waveforms. We thus verify the P_bs phases by a trail-and-error approach. After the candidate P_bs phase is picked, the arrivals of P_bpPs phase can be estimated (Equation 3). Then using the two initially picked values of P_bs and P_bpPs phases, the correctness of the phase identification can be verified by a posteriori information with independent observations (i.e., travel times of P and S waves).

For instance, there are coherent phases in region C between the first P arrival and the picked P_bs arrivals (Figure 2c). If this phase is treated as the candidate P_bs phase (blue line in Figure S2a), its corresponding P_bpPs phases are then determined (green line in Figure S2a). By repeating array-based inversion, we can obtain a LVZ model (Model B in Figures S2c1 and S2c2). By comparing this model with the H-κ result (blue dots in Figures S2c1 and S2c2) and the observed delay times of teleseismic P waves and S waves (Figures S2e1 and S2e2), we find that this model obviously overpredicted the travel times of P waves in region C (Figure S2e1). Similarly, if the coherent phase at ~5 s in region C is regarded as the P_bpPs phase (green line in Figure S2b), the predicted travel times of P waves significantly deviate from observations in region C (Figure S2f1). After a series of trial-and-error procedure, we conclude that the picked P_bs and P_bpPs phases in Figure 2c are the most appropriate ones.

3.2. RF Travel Time Inversion

In this study, we simply parameterize the multi-layered model to be one layer over a half-space, as we focus on the LVZ associated with the CHF. Such approach has been widely adopted in RF single-station method, such as the H-κ stacking method (Zhu & Kanamori, 2000), and has been demonstrated to be able to capture the main features of sedimentary effects (Langston, 2011). The effects of this simplification will be discussed in detail in Section 5.2.

Because there are two equations (Equations 1 and 2) with three unknowns (H, V_s, and κ) for the LVZ, some priori information, such as V_p or V_s of the LVZ, needs to be provided in the inversion (Zhu & Kanamori, 2000). Since the V_s model of the CHF in the upmost 2 km was robustly obtained by ambient noise tomography (Yang et al., 2020), we use the pre-determined V_s model in our studies.

According to Equations 1 and 2, for a certain station, the travel-time perturbation can be connected to the model parameter perturbation as the following,

$$\begin{pmatrix} \Delta t_{P_bs} \\ \Delta t_{P_bpPs} \end{pmatrix} = \begin{pmatrix} \frac{\partial t_{P_bs}}{\partial \kappa} & \frac{\partial t_{P_bs}}{\partial H} \\ \frac{\partial t_{P_bpPs}}{\partial \kappa} & \frac{\partial t_{P_bpPs}}{\partial H} \end{pmatrix} \begin{pmatrix} \Delta \kappa \\ \Delta H \end{pmatrix}, \tag{4}$$

where $\Delta t_{P_bs} = t^{\text{pre}}_{P_bs} - t^{\text{obs}}_{P_bs}$, $\Delta t_{P_bs} = t^{\text{pre}}_{P_bpPs} - t^{\text{obs}}_{P_bpPs}$, and the superscript *pre* and *obs* represent theoretical and observed travel times (P_bs or P_bpPs), respectively. The four partial derivatives in Equation 4 ($\frac{\partial t_{P_bs}}{\partial \kappa}, \frac{\partial t_{P_bs}}{\partial H}, \frac{\partial t_{P_bpPs}}{\partial \kappa}, \frac{\partial t_{P_bpPs}}{\partial H}$) are calculated analytically as shown in Appendix A. The predicted arrivals can be calculated using the assumed H and κ, combined with the pre-determined V_s model.

For notation simplification, hereinafter we refer t_{P_bs} and t_{P_bpPs} as t_1 and t_2, respectively. To formulate the array-based iterative inversion, we ensemble all the arrival times, partial derivatives, and unknown parameters for a single event in one equation. In addition, we also add the first-order Tikonov regularization smoothing operator (Aster et al., 2011) between adjacent stations. Assuming there are n stations in a seismic array, we have

$$\begin{pmatrix} \Delta \boldsymbol{t}_1 \\ \Delta \boldsymbol{t}_2 \\ \boldsymbol{0} \\ \boldsymbol{0} \end{pmatrix} = \begin{pmatrix} \boldsymbol{G}^{\boldsymbol{H}}_{\boldsymbol{t}_1} & \boldsymbol{G}^{\boldsymbol{\kappa}}_{\boldsymbol{t}_1} \\ \boldsymbol{G}^{\boldsymbol{H}}_{\boldsymbol{t}_2} & \boldsymbol{G}^{\boldsymbol{\kappa}}_{\boldsymbol{t}_2} \\ \lambda_H \boldsymbol{L} & \boldsymbol{0} \\ \boldsymbol{0} & \lambda_\kappa \boldsymbol{L} \end{pmatrix} \begin{pmatrix} \boldsymbol{H} \\ \boldsymbol{K} \end{pmatrix}, \tag{5}$$

where $\Delta \boldsymbol{t}_1 = \left[\Delta t_1^1, \cdots, \Delta t_1^i, \cdots, \Delta t_1^n\right]^T$, $\Delta \boldsymbol{t}_2 = \left[\Delta t_2^1, \cdots, \Delta t_2^i, \cdots, \Delta t_2^n\right]^T$,

$$\boldsymbol{G}^{\boldsymbol{H}}_{\boldsymbol{t}_1} = \text{diag}\left(\frac{\partial t_1^1}{\partial H}, \cdots, \frac{\partial t_1^i}{\partial H}, \cdots, \frac{\partial t_1^n}{\partial H}\right), \boldsymbol{G}^{\boldsymbol{\kappa}}_{\boldsymbol{t}_1} = \text{diag}\left(\frac{\partial t_1^1}{\partial \kappa}, \cdots, \frac{\partial t_1^i}{\partial \kappa}, \cdots, \frac{\partial t_1^n}{\partial \kappa}\right),$$

$$\boldsymbol{G}^{\boldsymbol{H}}_{\boldsymbol{t}_2} = \text{diag}\left(\frac{\partial t_2^1}{\partial H}, \cdots, \frac{\partial t_2^i}{\partial H}, \cdots, \frac{\partial t_2^n}{\partial H}\right), \boldsymbol{G}^{\boldsymbol{\kappa}}_{\boldsymbol{t}_2} = \text{diag}\left(\frac{\partial t_2^1}{\partial \kappa}, \cdots, \frac{\partial t_2^i}{\partial \kappa}, \cdots, \frac{\partial t_2^n}{\partial \kappa}\right),$$

$\boldsymbol{H} = \left[H_1, \cdots, H_i, \cdots, H_n\right]^T$ and $\boldsymbol{K} = \left[\kappa_1, \cdots, \kappa_i, \cdots, \kappa_n\right]^T$. In addition, $\boldsymbol{L}$ represents the first-order Tikonov regularization. λ_H and λ_κ are the smoothing parameters between adjacent 1-D models for H and κ, respectively.

After that, the standard damped least square inversion method (e.g., Marquardt, 1963) with travel times of P_bs and P_bpPs is used to estimate the depth extent and V_p/V_s ratio of the LVZ for all stations, simultaneously.

In this study, we assume that conversion points are located right below the stations, as the horizontal offset between the conversion point and the station is quite small. The horizontal offset could be calculated as $\Delta x = H * \tan\left(\arcsin\left(p * V_s\right)\right)$, where Δx is the offset, H is the estimated depth of the LVZ, p is ray parameter and V_s is the average shear wave velocity in the LVZ. Typically, the ray parameter p is 0.06 s/km, the depth of the LVZ model is 1.5 km and the S-wave velocity of the LVZ is 1 km/s, then the offset Δx is around 90 m. For comparison, the size of the Fresnel zone is $\frac{1}{2}\sqrt{\frac{V_s H}{f}} \approx 600$ m. The size of Δx is apparently smaller than that of size of the Fresnel zone, so it is neglectable in our inversion.

Note that the reliability of S-wave velocity model may largely affect our inversion results. In this study, we average the S-wave velocity beneath the LVZ (Figure 3b) (Yang et al., 2020). We choose the maximum S-wave velocity vertical gradient as the LVZ boundary, which roughly follows the velocity contour of 1.2 km/s (Figure 3a). We then compute the average S-wave velocity ($\bar{V}_s = H/\left(\int_0^H \frac{dz}{V_s}\right)$) upon the boundary depth beneath each station to build a reference LVZ shear wave velocity model (Figure 3b).

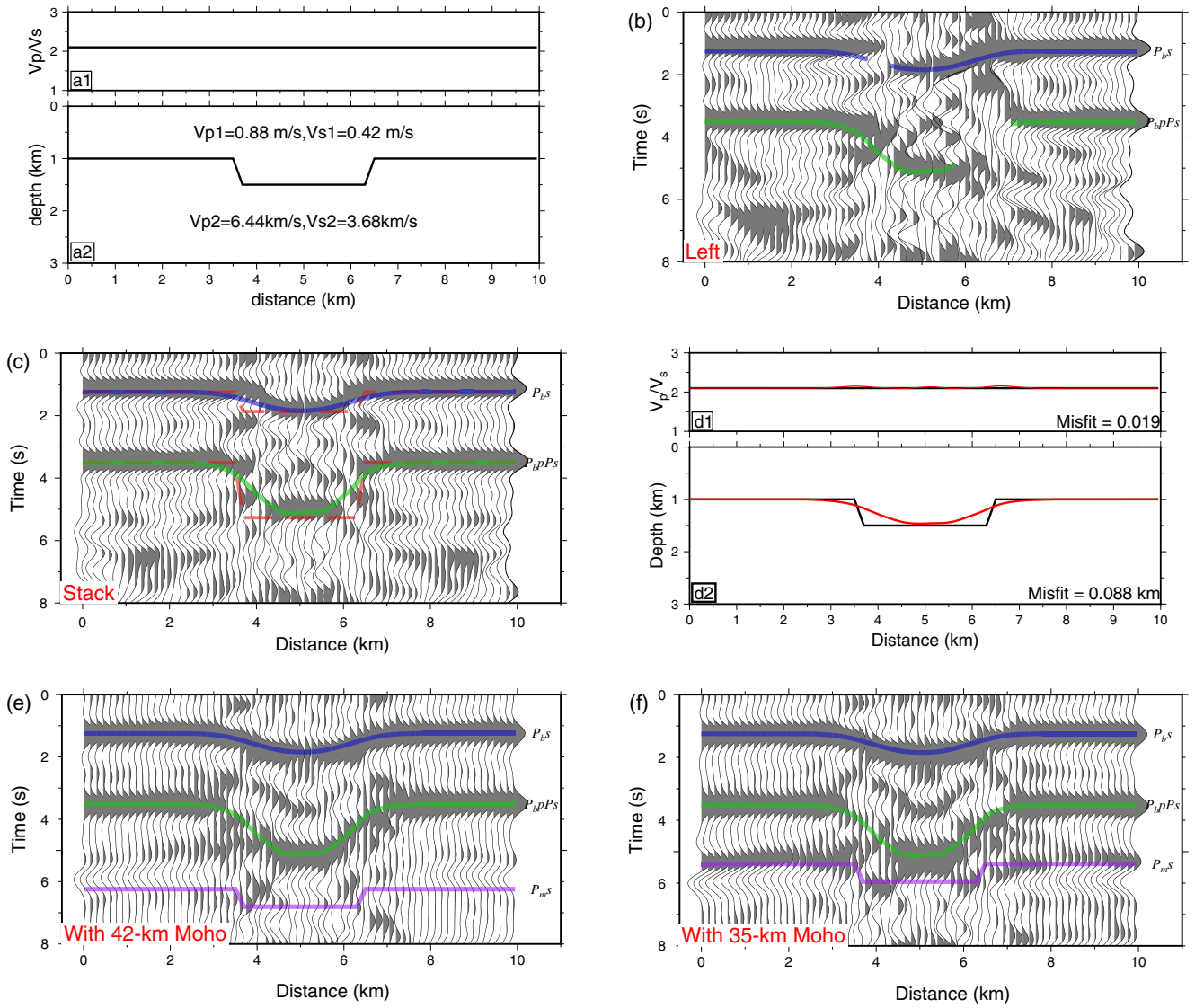

Figure 4. (al and a2) A hypothetical low-velocity-zone (LVZ) model with a 1.5-km sunken shape in the central part. (b) The corresponding synthetic receiver function (RF) waveforms resulting from one teleseismic event incident from the left bottom corner of the model in (a). (c) The stacked synthetic RFs of two events with opposite incidences. The blue and green solid lines denote the picked arrival time of P_bs and P_bpPs phases, respectively. The red dashed lines denote the theoretical arrivals of P_bs and P_bpPs. (d1 and d2) Synthetic array-based RF travel time inversion results. The red lines represent the inverted V_p/V_s ratio and depth extent of the LVZ. The black lines denote the corresponding true values. (e) The stacked RFs for the sunk LVZ model in (a) with a 42-km-depth Moho. (f) The stacked RFs for the sunk LVZ model in (a) with a 35-km-depth Moho. The purple solid lines in (e and f) denote the theoretical Moho P_ms arrival.

3.3. Synthetic Tests

We first perform several synthetic tests to demonstrate the reliability and robustness of our inversion method. The ground-truth model is constructed as a LVZ model with a 3-km-wide sunk in the central part from 1- to 1.5-km depth (Figure 4a). Based on the average *S*-wave velocity model in Figure 3b, V_s of the LVZ layer is set to 0.42 km/s, and V_p/V_s ratio is set to 2.1. The crust below the LVZ has the V_s of 3.68 km/s and V_p/V_s ratio of 1.75, respectively, based on the tomography results using a few explosion sources in the Binchuan region (S. Chen et al., 2016). There are 200 virtual receivers evenly distributed at the surface with a station spacing of 50 m in the *x*-axis direction.

Here we compute the synthetic seismograms resulting from planar incident *P* wave recorded by the receivers using a 2-D hybrid method (Tong et al., 2014), which uses a frequency-wavenumber integration method

(FK) to calculate analytical solutions using a 1-D layered background model and uses a spectral-element (SEM) numerical solver to provide synthetic responses of local media to plane-wave incidence. We then compute synthetic RFs from the seismograms using the time domain deconvolution method (Ligorria & Ammon, 1999) and low-pass filter RFs using the same Gaussian filter parameter of three, as used to process the data in Section 2.

Two teleseismic events from the opposite in-line directions with a ray parameter of 0.06 s/km are computed. RFs from a single event show clear P_bs and P_bpPs phases (Figure 4b). However, the amplitudes on one side of the sunk are quite weak and difficult to identify, which may result from the incident angle of plane wave at the LVZ interface (Figure 4b). We then stack RFs of the two events with opposite directions to weaken the effect of different incidences and to obtain enhanced *P*-to-*S* phases (Figure 4c). Then we pick P_bs and P_bpPs phases from the stacked RFs following the above process in Section 3.1. Our picked P_bs and P_bpPs arrivals (blue and green lines in Figure 4c) are consistent with the true arrivals (red dashed lines in Figure 4c). Because of diffractions near the sides of the sunk model, the arrivals are difficult to identify in the stacked RFs. Therefore, our picked arrivals are smoother than the true values at the two sides of the lateral steep change (Figure 4c).

In the inversion process, true ray parameter p of 0.06 s/km and V_s of 0.42 km/s are used, while the initial depth and V_p/V_s ratio are set to 1.5 km and 2.1, respectively. With picked arrivals of P_bs and P_bpPs phases (Figure 4c), we apply our inversion method (Equation 5). Here the first-order smoothing parameters (λ_H of 200 and λ_κ of 100) are added based on the L-curve tests (Section 4.1). When a minimum in misfit between observed and predicated arrivals is achieved after 200 iterations, we obtain the depth extent and V_p/V_s ratio (red lines in Figures 4d1 and 4d2). By comparing with true values of H and V_p/V_s ratio (black lines in Figures 4d1 and 4d2), the model can be largely recovered in the inversion result, with misfits of 0.088 km and 0.019 for depth and V_p/V_s ratio, respectively.

In the observed data, the converted phases from the Moho discontinuities may interfere with the multiples from the shallow structures, particularly the primary *P*-to-*S* converted waves (P_ms). Therefore, we conduct a further test to explore the effect of the multiples caused by the Moho discontinuities in our inversion. As shown in a RF result from a 2-D array in the same region (Jiang et al., 2020), the Moho depth in the Binchuan basin is ~42 km. Here we add a 42-km-depth Moho interface below the model in Figure 4a. The *S*-wave velocity and V_p/V_s ratio of the mantle are set to 4.48 km/s and 1.8, respectively, according to the results of active source tomography (S. Chen et al., 2016). All other parameters are the same to the first model. We also use the SEM-FK method to obtain stacked RFs of two events with opposite incidences. We then calculate theoretical P_ms arrivals (purple line in Figure 4e) based on the velocity model, which are ~1.5 s later than the P_bpPs phases caused by the LVZ. However, the amplitudes of the converted P_ms phases from the Moho discontinuity are weak, possibly due to the interference from multiples caused by the LVZ. In contrast, the waveforms of the P_ms phase have little effect on the P_bs and P_bpPs phases, so the targeted phases can be still clearly observed from the RF waveforms (Figure 4e). It is worth noting that in the existence of a shallower Moho (i.e., a 35-km-depth Moho), the arrival times of P_bpPs and P_ms phases beneath the LVZ may overlap with each, as shown in one of synthetic test models with a Moho depth of 35 km (Figure 4f). However, the Moho P_ms phases are still quite weak, and relatively strong P_bpPs phases are still able to be identified. Fortunately, the Moho depth in the Binchuan is well constrained by a larger-aperture dense array (Jiang et al., 2020) and the above synthetic tests demonstrate that the interference of the Moho P_ms phases will not affect the picking of arrival times of P_bs and P_bpPs phases.

Next, we carry out a further test to investigate the performance of our method on noisy data with the first LVZ model (Figure 4a). We add random white Gaussian noise to the teleseismic waveforms prior to deconvolution using the built-in function Add White Gaussian Noise (AWGN) within MATLAB. As such, a random time series, whose amplitude follows the Gaussian distribution, is added to each sampling point independently for the vertical and horizontal components of synthetic waveforms (Figure S3). The signal-to-noise ratio, which describes the energy ratio between the signal and the Gaussian white noise, is set to be −15 dB in the AWGN function. After the raw waveforms are calculated, with the same process as in Section 3.1, we calculate the RF waveforms, stack the waveforms, and pick P_bs and P_bpPs from stacked RFs (Figure 5a). Then we perform the array-based inversion and obtain corresponding results. Compared with the true model, the inverted depth and V_p/V_s ratio have misfits of 0.099 km and 0.081, respectively (Figure 5b).

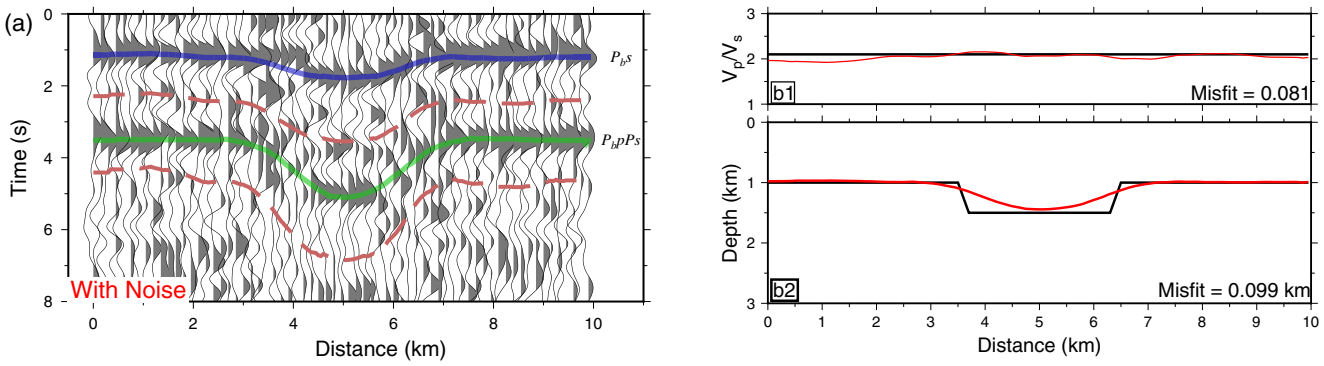

Figure 5. (a)The stacked synthetic receiver functions (RFs) with random Gaussian noise, which is added to the synthetic waveforms prior to deconvolution. The colored lines have the same meanings as Figure 2c. (b1 and b2) The corresponding RF travel time inversion results (red lines) with picked arrivals in (a).

This test indicates that our method can successfully recover the LVZ model even in the presence of noise, and the accuracy of the results may depend on the noise level. It is worth noting that the field data is usually much more complex, particularly because the noise level may vary significantly from station to station. To ensure the reliability of the inversion results, the arrival times need to be visually picked and measured on waveform data.

4. Results

4.1. Inversion of Thickness H and V_p/V_s Ratios

In order to stabilize the inversion results, the first-order smoothing constraint between adjacent 1-D models (λ_H for H and λ_κ for V_p/V_s ratio) are added in Equation 5 during the inversion. To determine the appropriate smoothing parameters, we perform L-curve tests to analyze the effects of the smoothing parameters on the trade-offs between the model roughness and travel-time data residuals (Figure 6). For $\lambda_H$we test 24 values ranging from 50 to 1,200 with an interval of 50, and 25 values between 20 to 500 with an interval of 20 for λ_κ. Figure 6a shows the values of model roughness and data residuals due to different smoothing parameter combinations. These values distribute approximately on a convex surface (Figure 6a). We then fix the λ_H and λ_κ to their "optimal" values, the intersection points of the two black lines in Figure 6a. More clearly, if one

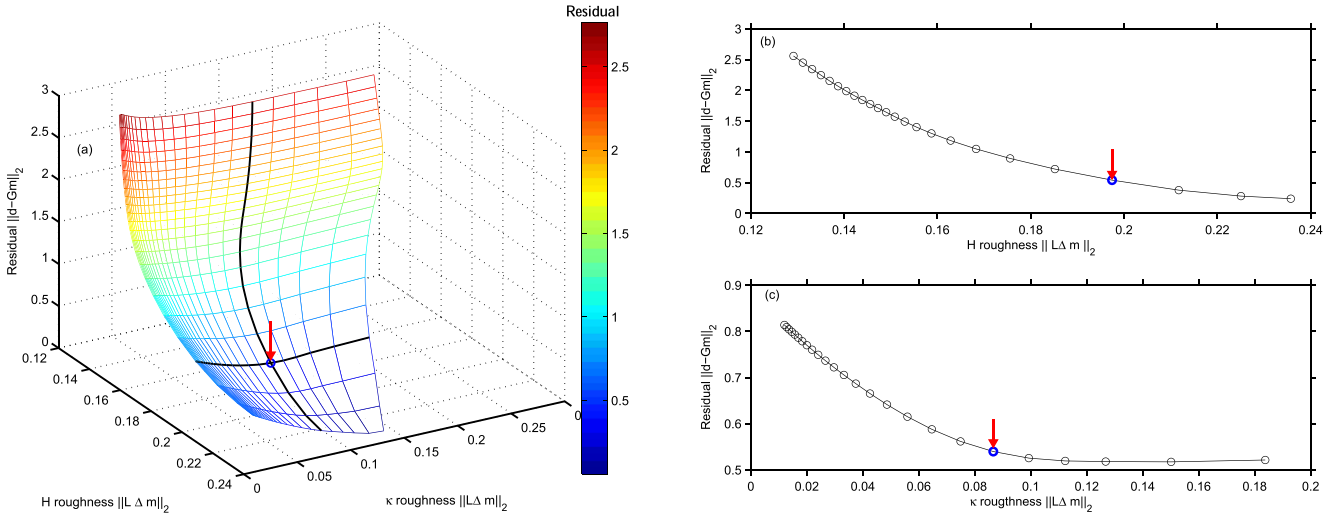

Figure 6. L-curve analysis to determine the appropriate smoothing parameters λ_H and λ_κ for inversion. (a) L-surface presenting the trade-off between the travel-time data residuals, H and κ model roughness. The two black curves intersect the point when one of two parameters is fixed. The colors represent the values of the travel-time data residuals. (b and c) L-curve for travel-time data residuals and model regularization and the parameters for H (b) and κ (c), respectively. The open blue circles (marked with red arrows) denote the "optimal" smoothing parameters selected for field data inversion.

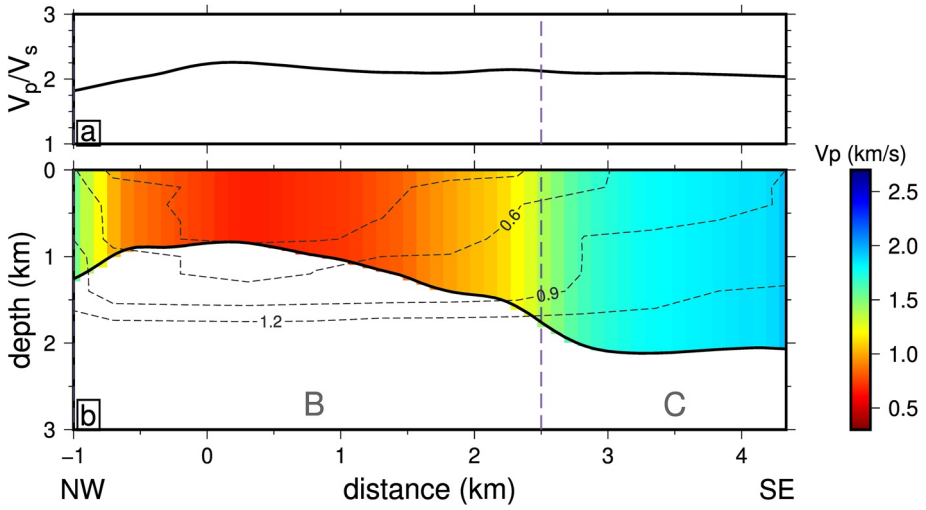

Figure 7. RF travel time inversion results for the linear dense array across the Chenghai Fault, (a) V_p/V_s ratio and (b) extent depth (black solid line) of the low-velocity-zone (LVZ). The *P*-wave velocity of the LVZ is calculated from the initial *S*-wave velocity and the resulting V_p/V_s in (a). The black dashed lines are V_s contours from Yang et al. (2020).

of the parameters is fixed, shaped L-curves are obtained for the two others (Figures 6b and 6c). Although the choice of parameters is subjective, the inversion results do not vary much around "optimal" λ_H and λ_κ of 200 and 120, respectively (marked with red arrows in Figures 6b and 6c). We provide an example to show the effects of several different smoothing parameter combinations on the inversion results in Appendix B.

For the picked P_bs and P_bpPs arrivals (Figure 2), we first interpolate them at a spacing of 40 m for the convenience of model regularization. Then, using the determined smoothing parameters, we apply the dense-array-based inversion method (Equation 5) with the interpolated arrivals to derive the depth extent and corresponding V_p/V_s ratio of the LVZ of the CHF. According to tomography results (Yang et al., 2020), we set initial depth of 1.5 km, κ of 2.25 and the average V_s model as the initial model (Figure 3b). When the misfit of travel times achieves its minimum after 500 iterations, we acquire optimal results of H and κ (Figure 7). From the V_p/V_s ratio and the V_s model, we also derive the corresponding V_p structure across the seismic array (Figure 7).

In our inversion result (Figure 7), the depth extent in region B increases from 0.8 to 1.7 km in the S-E direction, with an average value of 1.1 km. The V_p/V_s ratios in region B vary from 1.83 to 2.26, with the average value of 2.12. In region C, the depth extent ranges 1.8–2.1 km with an average of 2.0 km and the average V_p/V_s ratio is ~2.08. The depth extent of the LVZ in the inversion result (Figure 7) roughly coincides with the locations of a *S*-wave velocity vertical gradient extremum (approximately the velocity contours of ~0.4 km/s in Figure 3a) from the ambient noise tomography. It seems that the shape of the lower boundary of the LVZ from our inversion result varies more rapidly compared with the tomography result. Because the P_bs and P_bpPs phases constrain the velocity boundaries better than surface wave dispersion, and the model obtained in this study agree with the teleseismic *P* and *S* wave travel times (see Section 4.2 for details), we believe the model obtained in the current study is more reliable.

4.2. Comparison With *P*- and *S*-Waves Travel Times

In addition to the LVZ thickness, we obtain the *P*-wave velocity model using the V_p/V_s ratio and the initial V_s model. The average V_p values in regions B and C are ~0.91 and ~1.76 km/s, respectively (Figure 7). In order to verify the LVZ depth and velocity structure (Figure 7), we calculate theoretical *P*-wave arrivals for every station and then derive the across-array differential times relative to a reference station (located at the northwestern end of the region B).

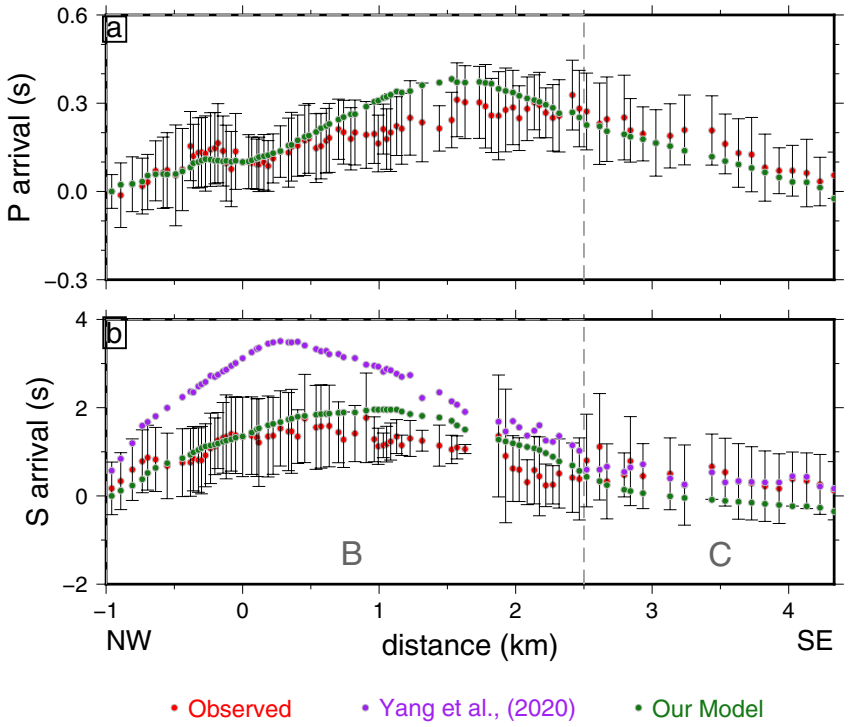

Figure 8. Observed and theoretical across-array delay times of (a) *P* waves and (b) *S* waves. The red dots denote observed relative delay times; the green dots denote predicted arrivals with our inversion model in Figure 7; the purple dots denote predicted arrivals from noise tomography model in Yang et al. (2020).

Here, we replace the shallow velocity parameters in the global CRUST1.0 model (Laske et al., 2013) with our inversion results (Figure 7) to calculate theoretical *P*-wave arrivals. To focus on the local structure, we correct the topographic effects using h_j/v_{ref}, where h_j are the elevations of individual stations (which vary less than 150 m across the seismic array) (Yang et al., 2020), and v_{ref} are the inverted *P*-wave velocities (Figure 7). We follow the same steps in Yang et al. (2020), but we use the inverted *P*-wave velocities as v_{ref} for each station. After that, we select the theoretical *P*-wave arrival time of one reference station (located at the northwestern end of the region B in Figure 8), and calculate theoretical relative *P*-wave arrivals for other stations (green dots in Figure 8a) with station geometry and topography correction, similar as in Yang et al. (2020).

We then derive the across-array differential *P* arrivals for every teleseismic event in observed data, and calculate the average values (red dots in Figure 8a) by removing their azimuthal effects and the array topography changes (Yang et al., 2020). As shown in Figure 8a, theoretical arrivals calculated from our new model (green dots) mostly match with observed *P* wave arrivals (red dots), which validates our picked phases in RFs and inverted results (Figure 7). In region B, our theoretical *P* wave arrivals over-predict the observations with ~0.1–0.2 s. This may be caused by the picking errors or the initial V_s errors, which will be discussed in Section 5.2.

Similar to the *P* waves, we calculate theoretical *S*-wave arrivals based on our inverted model following the similar procedure as in Yang et al. (2020). Then we compare the theoretical across-array *S*-wave differential times with the observations on the radial-component waveforms. We also correct the topographic and geometrical effects. As shown in Figure 8b, theoretical travel times of our inverted model (green dots) agree with observations within the range of observation uncertainties (red dots). The agreement between our model predictions with the observations are significantly improved than the predictions from the model of ambient noise tomography (Yang et al., 2020). Especially, the predictions of our inverted *S*-wave model agree with the observations much better in region B within the LVZ, whereas the theoretical arrival times predicted by the model obtained from ambient noise tomography (purple dots in Figure 8b) obviously over-predicted the travel time delays within the same region. As the depth sensitivity kernel in the noise tomography was less than 1 km (Yang et al., 2020), it probably overestimated the depth of the LVZ. In con-

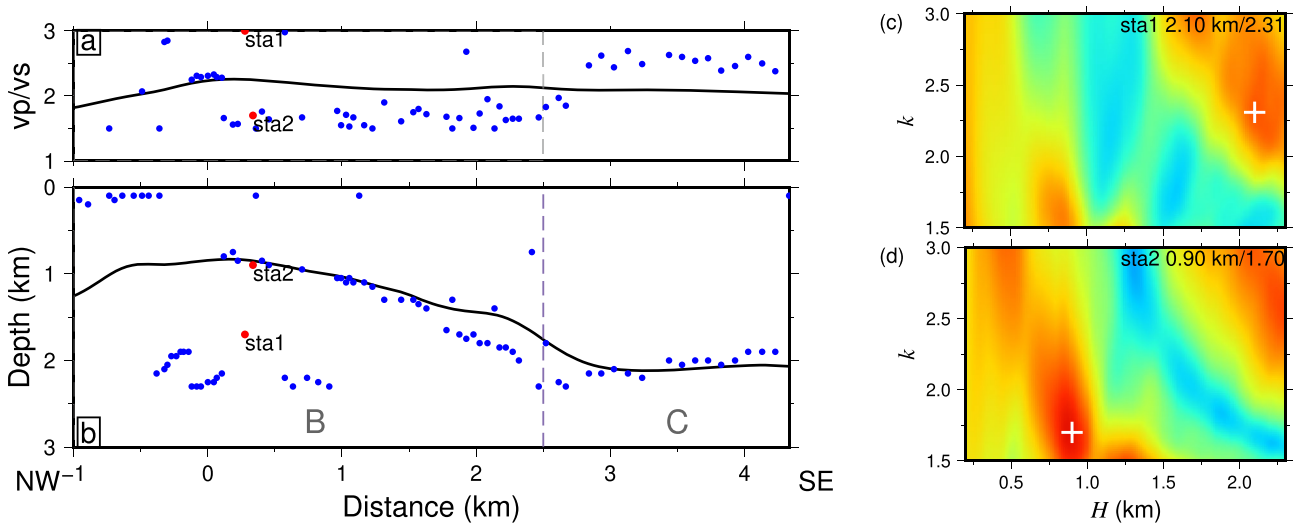

Figure 9. (a and b) Comparation between our results (solid lines) and the results from H-κ stacking method (blue dots). (c and d) The H-κ stacking images for two neighboring stations (red dots in [a]), where the cross symbols denote the best estimations on the low-velocity-zone depths and V_p/V_s ratios.

trast, our method is sensitive to the vertical velocity contrast, and thus can delineate the depth extent of the LVZ more precisely.

It is also noteworthy that the average V_p in region B seems unrealistically low (<1 km/s), which may be due to the following reasons. Because our focus is to constrain the bottom of the LVZ, we set up our model as one lay over a half space and only resolve an average V_p/V_s ratio, which may not perfectly describe region B as shown in the tomography results (Yang et al., 2020). First it cannot get rid of potential trade-off between the layer thickness and the average V_p/V_s ratio, despite our above approach. If our model underestimated the LVZ depth, then a slightly higher average value of V_p/V_s ratio will lead to the same predictions of travel times of P and S waves. Thus, the value of V_p in region B could be larger than 1 km/s. Alternatively, it is possible that the V_p/V_s ratio at much shallower depth in region B is much larger than our obtained average value, so that our approach here might underestimate the V_p values. To overcome such a problem, resolving the V_p/V_s ratio with higher resolution in the shallow depth, such as by borehole measurements or conducting an active source experiment, is demanded. But it is beyond the scope of this study.

5. Discussion

5.1. Comparison With H-κ Stacking Results

To compare our array-based RF travel-time inversion method with the single-station H-κ method, we also stack all the RFs recorded by each station and derive the depth extent and V_p/V_s ratio using the single-station H-κ stacking approach (Zhu, 2000). Since the S-wave velocities, rather than the P-wave velocities, are better constrained across the seismic array, we slightly modify the original H-κ method, and use S-wave velocities as the priori information. Because the H-κ method does not need P_bs and P_bpPs phases to be clearly identified, we have tried several Gaussian parameters and obtained similar results.

The H-κ stacking results on most stations (blue dots in Figures 9a and 9b) agree with our inverted results in a statistical sense (black lines in Figures 9a and 9b), further validating the results of our new method. On the other hand, compared with our results, the single-station H-κ results seem to be much more scattered. For instance, although the H-κ stacking diagrams (Figures 9c and 9d) seem quite similar for two neighboring stations (marked with red dots in Figures 9a and 9b), the depth and V_p/V_s ratio results vary significantly. This may be due to the fact that there are multiple local peaks in the H-κ domain (Figures 9c and 9d), and the algorithm may misidentify the peak in the single-station record. It is noteworthy that the H-κ results in region B are more scattered than those of region C (Figures 9a and 9b). According to the V_s model in Figure 2d, although region B is supposed to have larger velocity contrast than in region C, the lateral variation in

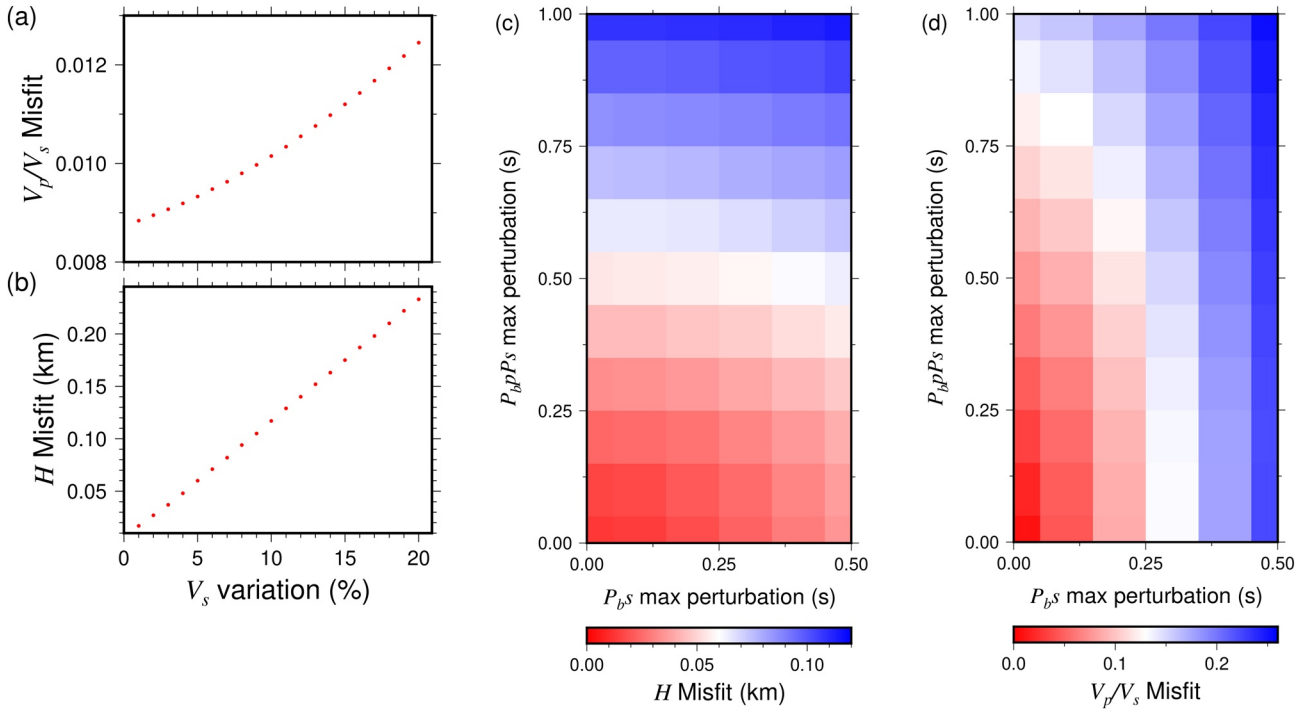

Figure 10. (a and b) Tests for *S*-wave velocity sensitivity for the depth and V_p/V_s ratio with the model in Figure 4a. (c and d) Tests for the influence of phase picking errors on the depth and V_p/V_s ratio for model in Figure 4a.

region B is also expected to be larger. Therefore, the *P*-to-*S* converted phases in region B seem more complicated than in region C (Figure 2c), leading to a more scattered distribution of the H-κ results in region B. In contrast, because our method inverts arrival times of all stations simultaneously with lateral smoothing constraint, the inverted subsurface structure appears to be more stable across the whole seismic array.

5.2. Sensitivity of *S*-Wave Velocity Variation

As noted previously, we use the simple model of one layer over a half space to parameterize the LVZ structure. This simplification has been used in many previous studies (e.g., Tao et al., 2014; Yeck et al., 2013; Y. Yu et al., 2015), and it is believed to be valid when the gradient of V_s is smaller than 1.5 km/s (Tao et al., 2014). We here calculate the difference between theoretical P_bs and P_bpPs arrivals from the multi-layered V_s model (Figure 2d) and its corresponding simplified model (Figure 3b), which are 0.063 and 0.163 s, respectively. Clearly the errors introduced by the model parameterization are far smaller than the picking errors (see Section 5.3). Therefore, the simple model of one layer over a half space can reasonably approximate the RF waveforms of a multi-layered model.

Furthermore, we investigate the effect of initial *S*-wave velocities on the array-based RF travel time inversion results. In the synthetic cases in Section 3.3, we use the ground-truth V_s model for inversion, which is probably not the case for the real data processing. To test the sensitivity of this method on the initial *S*-wave velocities, for the LVZ model in Figure 4a, we increase initial *S*-wave velocity from 1% to 20% with an interval of 1%. We use the theoretical P_bs and P_bpPs arrivals and keep other parameters unchanged, then apply the inversion method. From the inversion error analysis, the misfit of depth extent increases approximately by 0.01 km for every additional 1% for initial V_s model in deviation (Figure 10b). The misfit of depth is less than 0.23 km for the V_s deviations within 20%. The initial *S*-wave velocity deviations within 20% have a small effect on the V_p/V_s ratio, with the maximum misfit less than 0.013 (Figure 10a). In our data analysis, the error of V_s model derived by the ambient noise tomography (Yang et al., 2020) is less than 20%, which leads to uncertainties in depth extent and V_p/V_s ratio smaller than 0.2 km and 0.007, respectively.

5.3. Error Analysis of Picking P_bs and P_bpPs Arrivals

In the observational data, shallow multiple layers may result in a wider *P*-to-*S* phases and enlarge the errors of picking targeted phases. Here we explore the influence of the picking errors on the inversion results with the LVZ model in Figure 4a, by adding deviations to the arrivals of P_bs and P_bpPs phases. To do so, we add random noise to the phase picking arrivals, and the travel-time measure deviation from the ground-truth is randomly distributed within the maximum perturbation. For instance, if the maximum perturbation for the P_bs and P_bpPs arrivals is set to be 0.3 and 0.5 s respectively, we add ±0.3 s and ±0.5 s random errors to the true P_bs and P_bpPs arrivals for all receivers, respectively (see Figure S4). In this test, the ranges of maximum perturbation for the arrivals of P_bs and P_bpPs phases are 0–0.5 s and 0–1 s with an interval of 0.1 s, respectively.

The test results show that the misfit for the depth increases with the picking errors (Figure 10c), and the misfit reaches the maximum of 0.11 km with the maximum errors, i.e. ±0.5 s for P_bs phases and ±1 s for P_bpPs phases. The test also shows that the arrival perturbations have effects on the V_p/V_s ratio results with misfit less than 0.25 (Figure 10d). The misfit of the V_p/V_s ratios seems to be more sensitive to the P_bs arrivals perturbation than the P_bpPs perturbation (Figure 10d).

In the observed data for the dense array across the CHF, picking errors of the travel times of P_bs and P_bpPs vary in different regions. In the LVZ area (region B), the picking errors are expected to be smaller than in region C (Figure 2). Therefore, inverted results in region B are more robust and our main conclusions are not affected. In region C where velocities changed gradually in the vertical direction (Yang et al., 2020), the converted phases cannot be clearly identified (Figure 2c), leading to larger uncertainties in the inverted depth extent and V_p/V_s ratio.

5.4. Limitations and Other Applications of Our Method

We have demonstrated that our inversion method can not only obtain a more detailed lateral variation for depth extent of the shallow LVZ, but can also derive a *P*-wave velocity model of the LVZ, using the waveform records of teleseismic events on a dense array across the CHF. Although our results here refer to the LVZ, the method can be used to derive generic shallow structure of sedimentary layers with dense array data.

We also notice that there are some limitations of our method. First, densely distributed stations with three-component instruments are required to derive and track the coherent phases in RF waveforms. Nowadays dense arrays with nodal sensors grow rapidly, generating a large amount of dense-array data set. Although a number of large N arrays are composed of single-component sensors (e.g., Gradon et al., 2019; Schmandt & Clayton, 2013), limiting application of our method, there are numerous datasets acquired by three-component sensors (e.g., Ben-Zion et al., 2015; Jiang et al., 2020; Yang et al., 2021), which are capable of conducting array-based RF analysis.

Furthermore, the thickness of the shallow layer cannot be too thin that the P_bs and P_bpPs phases are not well separated in the frequency range. In addition, in order to apply our method successfully, a reliable 1-D V_s model beneath the array is needed. The V_s model can be derived by numerous approaches, such as using amplitudes of the first *P* waves in radial and vertical components to measure *S*-wave velocities (e.g., Ni et al., 2014; X. Wang et al., 2019), and ambient noise tomography (Yang et al., 2020). Integrating with our new method, reliable *P*-wave velocity model and depth extent of the shallow layer can be obtained so as to provide better understanding of fault zone structure and potential site amplification during earthquake shakings.

6. Conclusion

In this study, we develop a dense-array-based inversion method using RF travel times to simultaneously derive the depth extent and V_p/V_s ratio of the LVZ. Because the lateral smoothing constraint has been added in the inversion, this method results in more stable results compared with single-station method, such as the H-κ method. We conduct a series of synthetic tests to demonstrate the effectiveness and robustness

of this method. We also apply our proposed method to a linear dense seismic array across the CHF and identify the depth extent of 1.1 km of the LVZ, shallower than the previous result from ambient noise tomography (Yang et al., 2020). The average V_p/V_s ratio and V_p of the LVZ part are ~2.08 and 0.91 km/s, respectively. We compute the model predictions of across-array travel time delays for both P and S waves, and find they agree well with observations. With the increasing number of deployments of dense arrays, our dense-array-based RF travel time method can be a useful tool for shallow structure imaging in fault zones or sedimentary basins.

Appendix A: Analytical Partial Derivatives in Equation 4

From Equations 1 and 2, we can have the analytical partial derivatives of t_{P_bs} and t_{P_bpPs} to H and κ as,

$$\frac{\partial t_{P_bs}}{\partial H} = \sqrt{\frac{1}{V_s^2} - p^2} - \sqrt{\frac{1}{(V_s\kappa)^2} - p^2}, \tag{A1}$$

$$\frac{\partial t_{P_bs}}{\partial \kappa} = \frac{H}{V_s^2\kappa^3\sqrt{\frac{1}{(V_s\kappa)^2} - p^2}}, \tag{A2}$$

$$\frac{\partial t_{P_bpPs}}{\partial H} = \sqrt{\frac{1}{V_s^2} - p^2} + \sqrt{\frac{1}{(V_s\kappa)^2} - p^2}, \tag{A3}$$

$$\frac{\partial t_{P_bpPs}}{\partial \kappa} = -\frac{H}{V_s^2\kappa^3\sqrt{\frac{1}{(V_s\kappa)^2} - p^2}}, \tag{A4}$$

where H is the extent depth of LVZ, V_s is shear wave velocity, p is ray parameter, and κ is the V_p/V_s ratio.

Appendix B: The Tests for Effect of Smoothing Parameters to Inversion Results

To test the effect of the smoothing parameters on the inversion results in Figure 7, we compare inversion results with three different smoothing parameter combinations (λ_H, λ_κ). Since the optimal (λ_H,λ_κ) = (200, 120) (blue dots in Figure 6), we repeat the inversion two additional times using (λ_H,λ_κ) = (600, 500) and (1, 1) (Figure B1). Inversion results show that the smoothing parameters have little effect on the inversion results of depth extent, while the choice of λ_H and λ_κ affects the inversion of V_p/V_s ratio largely, especially near the boundary between the inferred low velocity and surrounding bedrock (Figure B1). Note that because the picked time in this study is smoothed before inversion, which can also smooth inversion results.

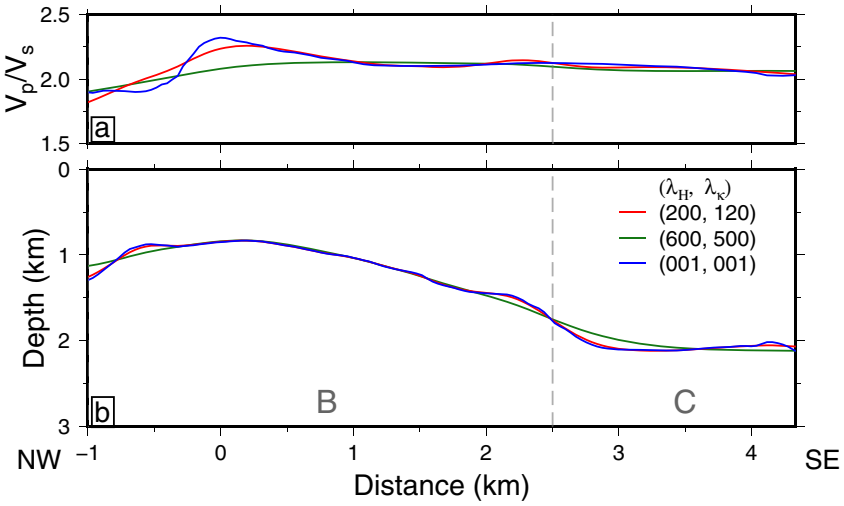

Figure B1. The effect of smoothing parameters (λ_H and λ_κ) on the inversion results. (a and b) The corresponding inversion results of V_p/V_s ratio (a) and the depth extent (b) used with the three different smoothing parameter combinations of (λ_H, λ_κ) as (200, 120), (600, 500) and (001, 001), respectively.

Data Availability Statement

Waveform data of the linear array used in this study are available from Data Management Centre of China Seismic Experimental Site (http://www.cses.ac.cn). Synthetic receiver function data used in this study can be found online (https://doi.org/10.5281/zenodo.4665757). The SEM-FK package is provided by Ping Tong of Nanyang Technological University, Singapore (Tong et al., 2014). MATLAB is available at (www.mathworks.com/products/matlab, last accessed March 2021).

Acknowledgments
This study is supported by the National Key R&D Program of China (2018YFC1503400), China Earthquake Science Experiment Project, CEA (grants no. 2018CSES0102, 2019CSES0107), HKSAR Research Grant Council GRF Grant 14305617, Faculty of Science, CUHK, and Chen Yong Academician Workstation of Yunnan Province in China (2014IC007).

References

Ampuero, J. P., Vilotte, J. P., & Sánchez-Sesma, F. J. (2002). Nucleation of rupture under slip dependent friction law: Simple models of fault zone. *Journal of Geophysical Research*, *107*(B12), 2324. https://doi.org/10.1029/2001JB000452

Aster, R., Borchers, B., & Thurber, C. (2011). *Tikhonov regularization, in parameter estimation and inverse problems* (2nd ed., pp. 93–127). New York: Elsevier Academic Press.

Avallone, A., Rovelli, A., Giulio, G. D., Improta, L., Ben-Zion, Y., Milana, G., & Cara, F. (2014). Waveguide effects in very high rate GPS record of the 6 April 2009, M_w 6.1 L'Aquila, central Italy earthquake. *Journal of Geophysical Research*, *119*, 490–501. https://doi.org/10.1002/2013/JB010475

Bao, Y., & Niu, F. (2017). Constraining sedimentary structure using frequency-dependent *P* wave particle motion: A case study of the Songliao Basin in NE China. *Journal of Geophysical Research*, *122*, 9083–9094. https://doi.org/10.1002/2017jb014721

Ben-Zion, Y., & Sammis, C. (2003). Characterization of fault zones. *Pure and Applied Geophysics*, *160*, 677–715. https://doi.org/10.1007/978-3-0348-8010-7_11

Ben-Zion, Y., Vernon, F. L., Ozakin, Y., Zigone, D., Ross, Z. E., & Meng, H. (2015). Basic data features and results from a spatially dense seismic array on the San Jacinto fault zone. *Geophysical Journal International*, *202*(1), 370–380. https://doi.org/10.1093/gji/ggv142

Brocher, T. M. (2005). Empirical relations between elastic wave speeds and density in the Earth's crust. *Bulletin of the Seismological Society of America*, *95*(6), 2081–2092. https://doi.org/10.1785/0120050077

Chen, S., Wang, B., Tian, X., Wang, F., Liu, B., & Li, L. (2016). Wide angle reflection and refraction results in Yunxian-Ninglang, north-western Yunnan (in Chinese). *Seismology and Geology*, *38*(1), 91–106. https://doi.org/10.3969/j.issn.0253-4967.2016.01.00

Chen, X., & Yang, H. (2020). Effects of seismogenic width and low-velocity zones on estimating slip-weakening distance from near-fault ground deformation. *Geophysical Journal International*, *223*. https://doi.org/10.1093/gji/ggaa385

Chen, X., Yang, H., & Jin, M. (2021). Inferring slip-weakening distance from near-fault accelerogram of the 2014 M_w 6.2 Ludian earthquake. *Seismological Research Letters*. https://doi.org/10.1785/0220210089

Cunningham, E., & Lekic, V. (2019). Constraining crustal structure in the presence of sediment: A multiple converted wave approach. *Geophysical Journal International*, *219*, 313–327. https://doi.org/10.1093/gji/ggz298

Cunningham, E., & Lekic, V. (2020). Constraining properties of sedimentary strata using receiver functions: An example from the Atlantic Coastal Plain of the southeastern United States. *Bulletin of the Seismological Society of America*, *110*, 510–533. https://doi.org/10.1785/0120190191

Duan, B., & Oglesby, D. D. (2007). Nonuniform prestress from prior earthquakes and the effect on dynamics of branched fault systems. *Journal of Geophysical Research*, *112*(B05), 308. https://doi.org/10.1029/2906JB004443

Gradon, C., Moreau, L., Roux, P., & Ben-Zion, Y. (2019). Analysis of surface and seismic sources in dense array data with match field processing and Markov chain Monte Carlo sampling. *Geophysical Journal International*, *218*(2), 1044–1056. https://doi.org/10.1093/gji/ggz224

Harris, R. A., & Day, S. M. (1997). Effects of a low-velocity zone on a dynamic rupture. *Bulletin of the Seismological Society of America*, *87*(5), 1267–1280.

Huang, X., Wu, Z., Huang, X., & Luo, R. (2018). Tectonic geomorphology constrains on quaternary activity and segmentation along Chenghai-Binchuan Fault Zone in Northwest Yunnan, China (in Chinese). *Earth Science*, *43*(12), 4651–4670. https://doi.org/10.3799/dqkx.2017.548

Huang, Y., & Ampuero, J. P. (2011). Pulse-like ruptures induced by low-velocity fault zones. *Journal of Geophysical Research*, *116*(B12) 307. https://doi.org/10.1029/2011JB008684

Huang, Y., Ampuero, J. P., & Helmberger, D. V. (2014). Earthquake ruptures modulated by waves in damaged fault zones. *Journal of Geophysical Research*, *119*, 3133–3154. https://doi.org/10.1002/2013JB010724

Huang, Y., Li, H., Liu, X., Zhang, Y., Liu, M., Guan, Y., & Su, J. (2020). The multiscale structure of the Longmen Shan central fault zone from local and teleseismic data recorded by short-period dense arrays. *Bulletin of the Seismological Society of America*, *110*, 1–11. https://doi.org/10.1785/0120190292

Jiang, X., Yang, H., Yang, W., & Wang, W. (2020). Crustal structure in the Binchuan Basin of Yunnan constrained from receiver functions on a 2-D seismic dense array. *Earthquake Science*, *33*, 264–272. https://doi.org/10.29382/eqs-2020-0264-01

Jiang, X., Zhu, L., Hu, S., & Huang, R. (2019). Three dimensional reverse time migration of teleseismic receiver functions using the phase-shift-plus-interpolation method. *Geophysical Journal International*, *271*(2), 1047–1057. https://doi.org/10.1093/gji/ggz066

Kame, N., Rice, J. R., & Dmowska, R. (2003). Effects of prestress state and rupture velocity on dynamic fault branching. *Journal of Geophysical Research*, *108*(B5), 2265. https://doi.org/10.1029/2002JB002189

Kennett, B. L. N., & Engdahl, E. R. (1991). Travel times for global earthquake location and phase association. *Geophysical Journal International*, *105*, 429–465. https://doi.org/10.1111/j.1365-246x.1991.tb06724.x

Kurzon, I., Vernon, F. L., Ben-Zion, Y., & Atkinson, G. (2014). Ground motion prediction equations in the San Jacinto Fault Zone: Significant effects of rupture directivity and fault zone amplification. *Pure and Applied Geophysics*, *171*(11). https://doi.org/10.1007/s00024-014-0855-2

Langston, C. A. (1979). Structure under Mount Rainier, Washington, inferred from teleseismic body waves. *Journal of Geophysical Research*, *84*(89), 4749–4762. https://doi.org/10.1029/jb084ib09p04749

Langston, C. A. (2004). Seismic ground motions from a bolide shock wave. *Journal of Geophysical Research*, *109*(B12) 309. https://doi.org/10.1029/2004JB003167

Langston, C. A. (2011). Wave-field continuation and decomposition for passive seismic imaging under deep unconsolidated sediments. *Bulletin of the Seismological Society of America*, *101*(5), 2176–2190. https://doi.org/10.1785/0120100299

Laske, G., Masters, G., Ma, Z., & Pasyanos, M. (2013). Update on CRUST1.0-A 1-degree global model of Earth's crust. In *Geophysical Research Abstracts* (EGU2013-2658) (Vol 15).

Lewis, M. A., Peng, Z., Ben-Zion, Y., & Vernon, F. L. (2005). Shallow seismic trapping structure in the San Jacinto fault zone near Anza, California. *Geophysical Journal of Intelligence*, *162*, 867–881. https://doi.org/10.1111/j.l365-246X.2005.02684.x

Li, Y. G., Leary, P., Aki, K., & Malin, P. (1990). Seismic trapped models in the Oroville and San Andreas fault zones. *Science*, *249*, 763–766. https://doi.org/10.1126/science.249.4970.763

Li, Y. G., Vidale, J. E., & Cochran, E. S. (2004). Low-velocity damaged structure of the San Andreas Fault at Parkfield from fault zone trapped waves. *Geophysical Research Letters*, *31*, L12S06. https://doi.org/10.1029/2003GL019044

Ligorria, J. P., & Ammon, C. J. (1999). Iterative deconvolution and receiver-function estimation. *Bulletin of the Seismological Society of America*, *89*(5), 1395–1400.

Lin, F., Li, D., Clayton, R. W., & Hollis, D. (2013). High-resolution 3D shallow crustal structure in Long Beach, California: Application of ambient noise tomography on a dense seismic array. *Geophysics*, *78*(4), 45–56. https://doi.org/10.1190/GEO2012-0453.1

Marquardt, D. W. (1963). An algorithm for least-squares estimation of nonlinear parameters. *Journal of the Society for Industrial and Applied Mathematics*, *11*(2). https://doi.org/10.1137/0111030

Mordret, A., Roux, P., Boué, P., & Ben-Zion, Y. (2019). Shallow three-dimensional structure of the San Jacinto fault zone revealed from ambient noise imaging with a dense seismic array. *Geophysical Journal International*, *216*, 896–905. https://doi.org/10.1093/gji/ggy464

Ni, S., Li, Z., & Somerville, P. (2014). Estimating subsurface shear velocity with radial to vertical ratio of local *P* waves. *Seismological Research Letters*, *85*(1), 82–90. https://doi.org/10.1785/0220130128

Oglesby, D. D., & Archuleta, R. J. (2000). Dynamics of dip-slip faulting: Exploration in two dimensions. *Journal of Geophysical Research*, *105*(B6), 13643–13653. https://doi.org/10.1029/2000jb900055

Oglesby, D. D., & Mai, P. M. (2012). Fault geometry, rupture dynamics and ground motion from potential earthquakes on the North Anatolian Fault under the Sea of Marmara. *Geophysical Journal International*, *188*, 1071–1087. https://doi.org/10.1111/j.1365-246X.2011.05289.x

Peng, Z., Ben-Zion, Y., Michael, A. J., & Zhu, L. (2003). Quantitative analysis of seismic fault zone waves in the rupture zone of the 1992 Landers, California earthquake: Evidence for a shallow trapping structure. *Geophysical Journal International*, *155*, 1021–1041. https://doi.org/10.1111/j.1365-246x.2003.02109.x

Roux, P., Moreau, L., Lecointre, A., Hillers, G., Campillo, M., Ben-Zion, Y., et al. (2016). A methodological approach towards high-resolution surface wave imaging of the San Jacinto Fault Zone using ambient-noise recordings at a spatially dense array. *Geophysical Journal International*, *206*, 980–992. https://doi.org/10.1093/gji/ggw193

Schmandt, B., & Clayton, R. W. (2013). Analysis of teleseismic *P* waves with a 5200- station array in Long Beach, California: Evidence for an abrupt boundary to Inner Borderland rifting. *Journal of Geophysical Research*, *118*, 1–19. https://doi.org/10.1002/jgrb.50370

Tao, K., Liu, T., Ning, J., & Niu, F. (2014). Estimating sedimentary and crustal structure using wavefield continuation: Theory, techniques and applications. *Geophysical Journal International*, *197*, 443–457. https://doi.org/10.1093/gji/ggt515

Tong, P., Chen, C., & Komatitsch, D. (2014). High-resolution seismic array imaging based on an SEM-FK hybrid method. *Geophysical Journal International*, *197*(1), 369–395. https://doi.org/10.1093/gji/ggt508

Vinnik, L. (1977). Detection of waves converted from P to SV in the mantle. *Physics of the Earth and Planetary Interiors*, *15*, 39–45. https://doi.org/10.1016/0031-9201(77)90008-5

Wang, B., Wu, G., Su, Y., Wang, B., Ge, H., Jin, M., et al. (2015). Site construction of the Binchuan transmitting seismic stations and preliminary observational data (in Chinese). *Journal of Seismological Research*, *38*(1), 1–6.

Wang, B. S., Yang, W., Wang, W., Yang, J., Li, X., & Ye, B. (2015). Diurnal and semidiurnal *P*- and *S*-wave velocity changes measured using an airgun source. *Journal of Geophysical Research*, *125*(1). https://doi.org/10.1029/2019JB018218

Wang, X., Chen, L., Gao, Y., Ling, Y., Zhang, J., & Yao, H. (2019). A new method to constrain shallow crustal *S*-wave velocities based on direct *P*-wave amplitudes in receiver functions and its application in northeastern Tibet. *Science China Earth Sciences*, *62*, 1819–1831. https://doi.org/10.1007/s11430-018-9443-6

Wang, Y., Lin, F., Schmandt, B., & Farrell, J. (2017). Ambient noise tomography across Mount St. Helens using a dense seismic array. *Journal of Geophysical Research*, *122*. https://doi.org/10.1002/2016JB013769

Ward, K. M., Lin, F., & Schmandt, B. (2018). High-resolution receiver function imaging across the Cascadia subduction zone using a dense array. *Geophysical Research Letters*, *45*(12). https://doi.org/10.1029/2018GL079903

Weng, H., Huang, J., & Yang, H. (2015). Barrier-induced supershear ruptures on a slipweakening fault. *Geophysical Research Letters*, *24*. https://doi.org/10.1002/2015GL064281

Weng, H., & Yang, H. (2018). Constraining frictional properties on fault by dynamic rupture simulations and near-field observations. *Journal of Geophysical Research*, *123*. https://doi.org/10.1029/2017JB015414

Weng, H., Yang, Z., Zhang, Z., & Chen, X. (2016). Earthquake rupture extents and co- seismic slips promoted by damaged fault zones. *Journal of Geophysical Research*, *121*(6), 4446–4457. https://doi.org/10.1002/2015JB012713

Wu, C., Peng, Z., & Ben-Zion, Y. (2009). Non-linearity and temporal changes of fault zone site response associated with strong ground motion. *Geophysical Journal International*, *176*, 265–278. https://doi.org/10.1111/j.1365-246X.2008.04005.x

Xu, Y., Koper, K. D., Burlacu, R., Herrman, R. B., & Li, D. (2020). A new uniform moment tensor catalog for Yunnan, China from January 2000 through December 2014. *Seismological Research Letters*, *91*(2A), 891–900. https://doi.org/10.1785/0220190242

Yang, H. (2015). Recent advances in imaging crustal fault zones: A review. *Earthquake Science*, *28*(2), 151–162. https://doi.org/10.1007/s11589-015-0114-3

Yang, H., Duan, Y., Song, J., Jiang, X., Tian, X., Yang, W., et al. (2020). Fine structure of the Chenghai fault zone, Yunnan, China constrained from tele- seismic travel time and ambient noise tomography. *Journal of Geophysical Research*, *125*. https://doi.org/10.1029/2020JB019565

Yang, H., Duan, Y., Song, J., Wang, W., Yang, W., Tian, X., & Wang, B. (2021). Illuminating high-resolution crustal fault zones and temporal changes using multi-scale dense arrays and airgun sources. *Earthquake Research Advances*. https://doi.org/10.19743/j.cnki.0891-4176.202101002

Yang, H., Liu, Y., & Lin, J. (2012). Effects of subducted seamounts on megathrust earthquake nucleation and rupture propagation. *Geophysical Research Letters*, *39*, L24,302. https://doi.org/10.1029/2012GL053892

Yang, H., Liu, Y., & Lin, J. (2013). Geometrical effects of a subducted seamount on stopping megathrust ruptures. *Geophysical Research Letters*, *40*, 1–6. https://doi.org/10.1002/grl.50509

Yang, H., Yao, S., He, B., & Newman, A. V. (2019). Earthquake rupture dependence on hypocentral location along the Nicoya Peninsula subduction megathrust. *Earth and Planetary Science Letters*, *520*, 10–17. https://doi.org/10.1016/j.epsl.2019.05.030

Yang, H., & Zhu, L. (2010). Shallow low-velocity zone of the San Jacinto fault from local earthquake waveform modelling. *Geophysical Journal International*, *183*, 421–432. https://doi.org/10.1111/j.1365-246X.2010.04744.x1

Yao, S., & Yang, H. (2020). Rupture dynamics of the 2012 Nicoya M_w 7.6 earthquake evidence for low strength on the megathrust. *Geophysical Research Letters*, *47*. https://doi.org/10.1029/2020GL087508

Yeck, W. L., Sheehan, A. F., & Schulte-Pelkum, V. (2013). Sequential H- stacking to obtain accurate crustal thicknesses beneath sedimentary basins. *Bulletin of the Seismological Society of America*, *103*(3), 2142–2150. https://doi.org/10.1785/0120120290

Yu, H., Liu, Y., Yang, H., & Ning, J. (2018). Modeling earthquake sequences along the Manila subduction zone: Effects of three-dimensional fault geometry. *Tectonophysics*, *733*, 73–84. https://doi.org/10.1016/j.tecto.2018.01.025

Yu, Y., Song, J., Liu, K., & Gao, S. (2015). Determining crustal structure beneath seismic stations overlying a low-velocity sedimentary layer using receiver functions. *Journal of Geophysical Research*, *120*, 3208–3218. https://doi.org/10.1002/2014JB011610

Zelt, B. C., & Ellis, R. M. (1999). Receiver-function studies in the Trans-Hudson Orogen, Saskatchewan. *Canadian Journal of Earth Sciences*, *36*, 585–603. https://doi.org/10.1139/e98-109

Zhang, J., & Gerstoft, P. (2014). Local-scale cross-correlation of seismic noise from the Calico fault experiment. *Earthquake Science*, *27*, 311–318. https://doi.org/10.1007/s11589-014-0074-z

Zhou, Q., Guo, S., & Xiang, H. (2004). Principle and method of delineation of potential seismic sources in northeastern Yunnan province (in Chinese). *Seismology and Geology*, *26*(4), 761–771.

Zhu, L. (2000). Crustal structure across the San Andreas Fault, southern California from teleseismic converted waves. *Earth and Planetary Science Letters*, *179*, 183–190. https://doi.org/10.1016/s0012-821x(00)00101-1

Zhu, L., & Kanamori, H. (2000). Moho depth variation in southern California from tele-seismic receiver functions. *Journal of Geophysical Research*, *105*, 2969–2980. https://doi.org/10.1029/1999jb900322

Zigone, D., Ben-Zion, Y., & Campillo, M. (2014). Seismic tomography of the Southern California plate boundary region from noise-based Rayleigh and Love waves. *Pure and Applied Geophysics*, *172*(5), 1007–1032. https://doi.org/10.1007/s00024-014-0872-1

Zigone, D., Ben-Zion, Y., Lehujeur, M., & Campillo, M. (2019). Imaging subsurface structures in the San Jacinto fault zone with high-frequency noise recorded by dense linear arrays. *Geophysical Journal International*, *217*, 879–893. https://doi.org/10.1093/gji/ggz069